



Origins of the intraseasonal variability contributing to the extreme rainfall in Henan Province of China in July 2021

Sihua Huang¹ · Zhiping Wen^{1,2,3,4} · Xiaodan Chen¹ · Yuanyuan Guo¹ · Zhewen Wang⁵

Received: 10 June 2023 / Accepted: 28 November 2023 / Published online: 5 January 2024
© The Author(s), under exclusive licence to Springer-Verlag GmbH Germany, part of Springer Nature 2024

Abstract

The present study investigates characteristics and origins of the intraseasonal oscillation (ISO) contributing to the extreme rainfall in Henan Province, China in July 2021. Significant 10–30-day and 30–60-day ISOs feature the extreme rainfall in Henan and jointly account nearly 52% for the total rainfall from 17 to 22 July. The related intraseasonal low-level circulations exhibit a meridional dipole pattern with a cyclonic anomaly over the western North Pacific and an anticyclonic anomaly over the Northeast Asia, which originate from the tropical and mid-to-high latitude ISO forcings in the upper and lower level. While the northwestward/northward-propagating Boreal Summer ISO (BSISO) and the mid-to-high latitude wave train contribute to the southern and northern nodes of the dipole pattern, respectively, the preceding cold sea surface temperature (SST) anomaly over the Sea of Japan and Kuroshio Extension region further strengthens the northern node through stabilizing the atmosphere and suppressing the convective activity. It is noteworthy that the concurrence of the 30–60-day BSISO and the mid-latitude SST anomaly could facilitate the BSISO convection to propagate further north and intrude the mid-latitude region. This unique relationship is infrequent in the past forty years with an occurrence probability of only 7.8% and tends to occur under the warmer-than-normal SST mean state in the mid-latitude North Pacific. The present study highlights the influence of the mid-latitude SST anomaly involved in the intraseasonal air-sea interaction, which may also be a potential precursor for the subseasonal prediction of the extreme rainfall in Henan.

Keywords Extreme rainfall · Intraseasonal oscillation · Tropical boreal summer intraseasonal oscillation · Mid-latitude sea surface temperature

1 Introduction

Extreme rainfall is one of the natural disasters that have catastrophic influences on society and human. It is reported that extreme rainfall events are becoming intensified and frequent under the global warming scenario (IPCC 2021), which would increase risks of urban waterlogging and torrential flooding. However, state-of-the-art models have limited skills in predicting extreme rainfalls due to the complex mechanisms of extreme rainfalls (Liu et al. 2020; Wu et al. 2023; Yan et al. 2023). A better understanding of the underlying mechanism responsible for extreme rainfalls is critical for improving extreme weather forecasts and enhancing precautions against disasters.

During the late July in 2021, Henan Province, located in the eastern-central China, suffered an unprecedentedly extreme rainfall event, which caused devastating floods and hundreds of victims. It is reported that the synergistic effect of various scales of atmospheric circulations, especially

✉ Zhiping Wen
zpw@fudan.edu.cn

¹ Department of Atmospheric and Oceanic Sciences and Institute of Atmospheric Sciences, Fudan University, Shanghai 200438, China

² Shanghai Key Laboratory of Ocean-Land-Atmosphere Boundary Dynamics and Climate Change, Fudan University, Shanghai 200438, China

³ Institute of Eco-Chongming (IEC), 20 Cuiniao Rd., Chongming, Shanghai 200062, China

⁴ Jiangsu Collaborative Innovation Center for Climate Change, Nanjing 210023, China

⁵ Zhumadian Meteorological Office, Zhumadian 463000, China

the western North Pacific subtropical high (WNPSH) and Typhoon In-Fa and Cempaka, greatly contributes to this extreme rainfall event (Ran et al. 2021; Su et al. 2021; Liang et al. 2022; Xu et al. 2022a, b). The northward-shift WNPSH and Typhoon In-Fa generate a large pressure gradient near 30°N over the subtropical western North Pacific and thus a strong low-level easterly jet. Abundant water vapor supplied by Typhoon In-Fa are transported into Henan by the low-level jet (Nie and Sun 2022; Xu et al. 2022c). Subsequently, anomalously strong moisture convergence occurs in central and northern Henan due to the block of the Taihang Mountain and Funiu Mountain in western Henan, accompanied by the strong uplift along the east edge of the mountains, ultimately leading to the occurrence of the extreme rainfall (Ran et al. 2021; Zhang et al. 2021; Liang et al. 2022).

While large-scale atmospheric circulations provide favorable dynamic and thermodynamic conditions for the extreme rainfall, the intraseasonal oscillation (ISO), the dominant source for the subseasonal climate predictability, plays a direct role in the duration and intensity of the extreme rainfall event in East Asia (Zhu et al. 2003; Mao and Wu 2006; Sun et al. 2016; Ren et al. 2018; Wang et al. 2022), with the extreme rainfall event in Henan no exception. Hsu et al. (2023) pointed out that the Henan flooding in July 2021 is enhanced and maintained by the 10–30-day and 30–90-day atmospheric ISOs. The atmospheric ISOs manifest a meridional dipole pattern at the lower level, characterized by an anticyclonic anomaly over the northeastern Asia and a cyclonic anomaly over the subtropical western North Pacific. The related ISO flows cause strong moisture convergence anomalies in conjunction with the increased mean-state moisture condition, contributing to the extreme rainfall in Henan. However, subseasonal-to-seasonal models underestimate this extreme rainfall event, which results from the biases in the ISO flow intensity and multiscale interactions. Since the ISO flows are closely related to the low-level meridional dipole pattern, it is possible that the poor prediction skill of models stems from the misrepresentation in reproducing the intraseasonal dipole pattern. Besides, Hu et al. (2023) pointed out that the unpredictable component of such a meridional dipole pattern on seasonal time scale in July 2021, explaining nearly 72% variance of the observed northward shift of the WNPSH, is related to the atmospheric ISOs. It hints a necessary to explore the origins of the intraseasonal meridional dipole pattern responsible for the unprecedented extreme rainfall in Henan, which will extend previous understandings of the mechanism causing extreme rainfalls and offer an opportunity for the extended-range forecast.

It has been demonstrated that the ISOs related to extreme rainfalls primarily originate from the tropical and extratropical forcings (e.g., Li et al. 2021; Liu et al. 2021, 2022; Gao et al. 2022; Ren et al. 2022; Nie and Sun 2023). Liu et al.

(2022) provided a comprehensive understanding on the origins of the ISO of global land summer monsoon rainfall and found differences in the origins in different monsoon regions. In East Asian monsoon region, the high-frequency ISO (8–20 days) mainly stems from the convectively coupled equatorial waves that propagates northwestward from the tropical western Pacific and the southeastward-propagating mid-latitude wave train, while the low-frequency ISO (20–70 days) is related to the northward propagating ISO that originates from the Indian Ocean. The tropical ISO signals are tightly related to the boreal summer ISO (BSISO), which consists of a 30–60-day component (also refers as BSISO1) and a 10–30-day component (also refers as BSISO2) (Annamalai and Slingo 2001; Kemball-Cook and Wang 2001). The tropical enhanced (suppressed) convections associated with these BSISO modes can exert anomalous easterlies (westerlies) as Kelvin-wave responses to its east and a pair of anomalous cyclones (anticyclones) as Rossby-wave responses to its west, manifesting a convectively coupled Kelvin-Rossby wave packet (Gill 1980). These coupled convection-circulation systems further propagate northward or northwestward in the form of a Rossby wave-like pattern (Wang and Xie 1997) and have great impacts on rainfalls over Yangtze River Basin through the abundant moisture transport by the anomalous southwesterlies along the northwestern flank of the anomalous anticyclone over the South China Sea-Philippine Sea (Li et al. 2015). The BSISO-related convection can also induce a meridional-vertical cell with the anomalous ascending branch over the central-eastern China, thus contributing to the rainfall extreme there (Chen and Zhai 2017; Li and Mao 2019a).

The extratropical signal responsible for the ISO of summer rainfalls in East Asia is usually linked to the mid-latitude Rossby wave train that propagates along the westerly jet stream (e.g., Yang et al. 2010; Liu et al. 2021; Gao et al. 2022; Guan et al. 2022; Ren et al. 2022). The mid-latitude wave train commonly exhibits a barotropic structure, but the phase propagation direction ranges from the eastward propagation, the westward propagation and nearly stationary (Ding and Wang 2007; Yang et al. 2013; Du and Lu 2021). When the intraseasonal wave train reaches East Asia, it can affect the vertical motion over the Yangtze River Basin via upper-level vorticity advections, thus causing heavy rainfall therein (Yang et al. 2010; Li and Mao 2018, 2019b). Guan et al. (2022) also pointed out that the upper-level cyclonic and anticyclonic anomalies embedded in the 10–20-day intraseasonal wave train favor the anomalous upward motion and the low-level southerly, prompting persistent extreme rainfalls in North China.

Since Henan Province locates in the subtropical region, the extreme rainfall over there is supposed to be influenced by the forcings from the tropics and the mid-to-high latitude

region. By far, how these tropical and extratropical signals take effects on the extreme rainfall in Henan in July 2021 remains to be unraveled. Therefore, the aim of the present study is to investigate how these signals affect the intraseasonal large-scale circulations and thus the extreme rainfall event in Henan in July 2021, which includes the influence of the BSISO, the mid-to-high latitude wave train and the mid-latitude sea surface temperature (SST) anomaly involved in the air-sea interaction.

2 Data and methods

2.1 Data

The data used in the present study include: (1) The daily mean rainfall records from 1 May to 28 September 2021 provided by the Information Centre of Henan Meteorological Service, which are calculated by averaging the daily rainfall across 121 national meteorological stations in Henan Province; (2) The twice-per-day (sampling at 0000 and 1200 UTC) variables from the fifth generation of European Centre for Medium-Range Weather Forecasts atmospheric reanalysis data (ERA5; Hersbach et al. 2020), including the three-dimensional winds, geopotential height, specific humidity, air temperature, total precipitation, total cloud cover, short-wave radiation, and surface latent heat flux (downwards positive). The period is from 1 January 1979 to 31 December 2021 and the horizontal resolution is $1^\circ \times 1^\circ$. The daily mean is computed by averaging the twice-per-day data in each calendar day; (3) The SST data from the version 2.1 of the National Oceanic and Atmospheric Administration (NOAA) Optimum Interpolation Sea Surface Temperature (OISST), which is based upon the Advanced Very High Resolution Radiometer (AVHRR) satellite (Reynolds et al. 2007). The SST data is available at $0.25^\circ \times 0.25^\circ$ resolution and is then interpolated into a $1^\circ \times 1^\circ$ resolution; (4) The daily mean outgoing longwave radiation (OLR) from NOAA

2.2 Methods

To extract intraseasonal signals, the data are pre-processed by the following steps. First, anomalous values are obtained after the removal of the seasonal evolution (i.e., climatological mean of each calendar day from 1991 to 2020) from the original data. The synoptic-scale signals are then eliminated by subtracting the 5-day running mean of the anomalous values. Finally, a 10–30- and a 30–60-day band-pass Lanczos filter (Duchon 1979) with 61 points weighted are utilized to grab the intraseasonal signals. The band-pass filter is performed on the observed rainfall records from May to September due to the limited data length, but from January to December for the reanalysis data. It would not yield significant differences if applying that on the reanalysis data from May to September.

The Monte Carlo test is carried out to examine the significance of the daily anomalies in July 2021 compared to those in the historical period. We randomly select one sample from the daily values in July from 1991 to 2020 and repeat it for 1000 times. These 1000 values are then ranked in an ascending order. The anomaly is considered to be statistically significant at the 90% confidence level if it is larger than the 950th value or smaller than the 50th value. For the composite result in Sect. 4, statistically significant analysis is applied by using the Student’s *t*-test.

We explore the moisture supply associated with extreme rainfalls through the column-integrated moisture flux, which is defined as:

$$\bar{Q}_x = -\frac{1}{g} \int_{p_s}^{p_t} q u dp, \quad \bar{Q}_y = -\frac{1}{g} \int_{p_s}^{p_t} q v dp, \tag{1}$$

where \bar{Q}_x and \bar{Q}_y are the zonal and meridional components of column-integrated moisture flux. u, v, q are the zonal, meridional wind, and specific humidity. p_s represents the surface pressure and $p_t = 300hPa$. g is the gravitational acceleration.

To describe the propagation of Rossby wave energy, the wave activity flux (WAF) is examined following Takaya and Nakamura (2001):

$$F_{TN} = \frac{p \cos \varphi}{2|\mathbf{U}|} \left(\begin{array}{l} \frac{U}{a^2 \cos^2 \varphi} \left[\left(\frac{\partial \psi'}{\partial \lambda} \right)^2 - \psi' \frac{\partial^2 \psi'}{\partial \lambda^2} \right] + \frac{V}{a^2 \cos \varphi} \left[\frac{\partial \psi'}{\partial \lambda} \frac{\partial \psi'}{\partial \varphi} - \psi' \frac{\partial^2 \psi'}{\partial \lambda \partial \varphi} \right] \\ \frac{U}{a^2 \cos \varphi} \left[\frac{\partial \psi'}{\partial \lambda} \frac{\partial \psi'}{\partial \varphi} - \psi' \frac{\partial^2 \psi'}{\partial \lambda \partial \varphi} \right] + \frac{V}{a^2} \left[\left(\frac{\partial \psi'}{\partial \varphi} \right)^2 - \psi' \frac{\partial^2 \psi'}{\partial \varphi^2} \right] \end{array} \right) \tag{2}$$

Interpolated Outgoing Longwave Radiation dataset with a resolution of $2.5^\circ \times 2.5^\circ$ (Liebmann and Smith 1996).

F_{TN} represents the horizontal WAF. $p = \text{pressure}/1000hPa$, and a is the earth’s radius, $\mathbf{U} = (U, V)$ is the background horizontal wind. $\psi = \frac{\Phi}{p}$ is the geostrophic stream function where Φ is geopotential. The primes represent the 10–30-day or 30–60-day ISO component.

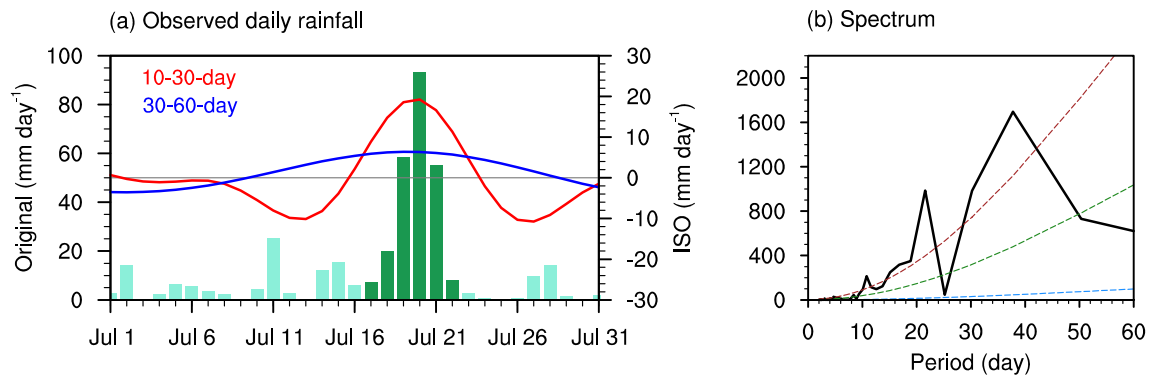


Fig. 1 **a** Time series of the observed daily rainfall averaged across Henan Province (bar; mm day^{-1}) and its 10–30-day (red curve) and 30–60-day components (blue curve) in July 2021. Bars in dark green mark the rainfall from 17 to 22 July. **b** Power spectrum of the

observed daily rainfall in Henan from May to September 2021. The green, red, and blue dash curves denote the Markov red noise spectrum, the 95% and 5% confidence levels, respectively

3 Characteristics of ISOs of the extreme rainfall in Henan and atmospheric circulations in July 2021

Figure 1a shows the temporal evolution of the daily rainfall averaged across Henan Province. The extreme rainfall event onsets on 17 July and ends on 22 July, lasting for 6 days (Liang et al. 2022). The heaviest rainfall occurs on 20 July with an amount of 93.0 mm, followed by considerable rainfall on 19 July (58.5 mm) and 21 July (54.9 mm). The averaged intensity of this long-persistent extreme rainfall from 17 to 22 July reaches 40.2 mm day^{-1} , nearly 7.7 times of the climatological mean rainfall across Henan in July ($\sim 5.2 \text{ mm day}^{-1}$).

Power spectrum analysis of the observed daily rainfall in Henan (Fig. 1b) shows that the Henan rainfall in summer 2021 exhibits two salient ISO periods, that is, 10–30 days and 30–60 days. The positive phases of both intraseasonal modes enhance and overlap from mid to late July, concurrent with the extreme rainfall in Henan (Fig. 1a), suggesting that the long duration of the extreme rainfall in Henan could be attributed to the concurrence of wet phases of ISOs. The relative contribution of 10–30-day and 30–60-day ISOs to total rainfalls from 17 to 22 July (calculated by the ratio of the intraseasonal rainfall amount to original rainfall amount) is nearly 37% ($\approx 14.9 \text{ mm day}^{-1}/40.2 \text{ mm day}^{-1}$) and 15% ($\approx 6.1 \text{ mm day}^{-1}/40.2 \text{ mm day}^{-1}$), respectively, jointly explaining more than half of total rainfalls ($\sim 52\%$) in Henan. This contribution is smaller than that suggested in Hsu et al. (2023) ($\sim 86\%$), which may be due to that they used reanalysis datasets and a wider band of intraseasonal time scale (10–90 days). As a comparison, the ratio of the synoptic-scale component to total rainfalls is nearly 39% from 19 to 21 July, coherent with Huang et al. (2022), but only 6% from 17 to 22 July.

The 10–30-day and 30–60-day filtered circulations at the lower level during the extreme rainfall period (17 to 22 July) share an analogously meridional dipole pattern (Fig. 2a, b), which is characterized by a cyclonic low anomaly over the western North Pacific and an anticyclonic high anomaly over Northeast China and Japan, in line with Hsu et al. (2023). Nonetheless, obvious differences exist in the intensity and distribution of the dipole pattern between two ISO modes. The amplitude of the 10–30-day filtered dipole pattern is obviously stronger, and the extensive anticyclonic anomaly is composed by two parts: the west one over the Northeast China with a northeast-southwest-tilted distribution and the east one over Japan and the adjacent ocean (Fig. 2a). The 30–60-day ISO mode is relatively weaker and exhibits a zonal-elongated distribution. Accordingly, anomalous easterlies ($\sim 30^\circ\text{N}$) between the anticyclonic and cyclonic anomalies are stronger in the 10–30-day ISO mode than in the 30–60-day ISO mode, and thus lead to more enhanced moisture transports from Pacific Ocean to inland and stronger moisture convergence anomaly in central and northern Henan in 10–30-day ISO mode (Fig. 2c, d). This westward water vapor channel also occurs during the extreme rainfall in Henan in August 1975, which is formed by the strong easterly anomaly in the north of the super Typhoon Nina (e.g., Ding 2015; Rao et al. 2022). However, compared to other rainstorm days with the Henan rainfall exceeding the 90th percentile in July from 1979 to 2020, this kind of strong westward moisture channel to the east of Henan is rarely found (Fig. S1c). Wang and Liu (2017) demonstrated that the extreme rainfall in Henan could be caused by the eastward-moving southwest vortex and the southwesterly flow. The composite circulation anomaly at lower level during the rainstorm days also shows a vortex anomaly southwest to Henan (Fig. S1a), which may be linked to the southwest vortex that forms in the Southwest China (Fu et al. 2013; Zhong et al. 2014). It suggests a unique role of the dipole

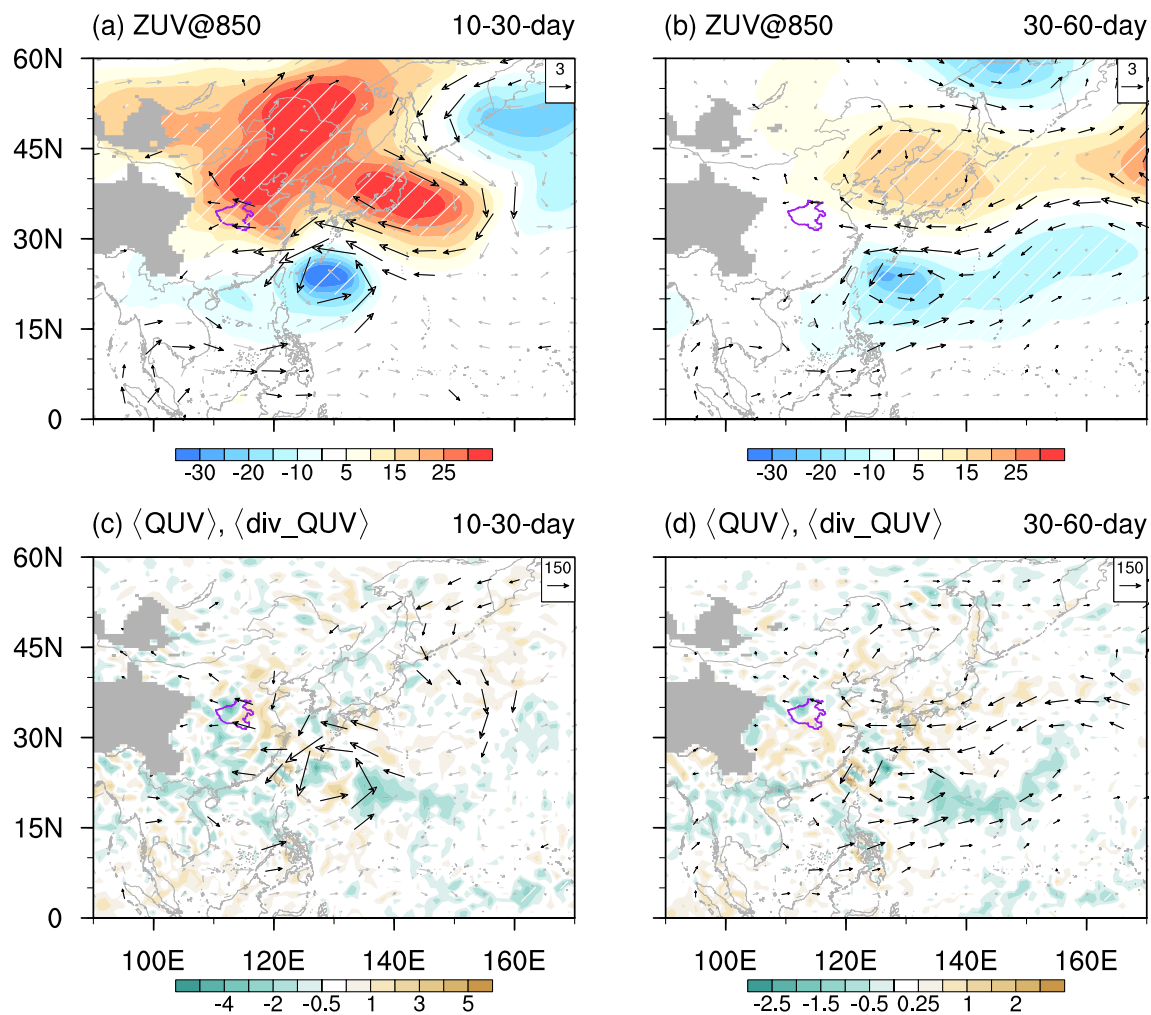


Fig. 2 10–30-day (left panel) and 30–60-day (right panel) ISO components of **a, b** the 850-hPa geopotential height (shaded; gpm), horizontal winds (vector; m s^{-1}), **c, d** column-integrated moisture flux (vector; $\text{kg m}^{-1} \text{s}^{-1}$) and divergence (shaded; $10^{-4} \text{ kg m}^{-2} \text{s}^{-1}$) averaged over 17 to 22 July. Henan Province is outlined in purple. The black vectors and the white oblique lines denote significant at the 90% confidence level using Monte Carlo test

pattern in the Henan extreme rainfall in July 2021 and calls again for a deeper understanding on how this intraseasonal dipole pattern generates and maintains.

Figure 3 displays the spatial–temporal evolution of the low-level atmospheric circulations in the 10–30-day and 30–60-day ISO modes responsible for the extreme rainfall in Henan. The day of the heaviest rainfall (20 July) is referred to as D0 and days leading (lagging) D0 are labeled as D–1, D–2, D–3, ... (D+1, D+2, D+3, ...) accordingly. It is interesting to find that the intense anticyclonic anomaly of the 10–30-day filtered dipole pattern results from three small anticyclonic anomalies. The first one is the anticyclonic anomaly (A1) emerging on D–6 over the Kuroshio Extension region (~40°N). It then approaches toward Northeast China on D0. The second one is the small-scale anticyclonic anomaly (A2) originating from the anticyclonic anomaly over the South China Sea and Philippine Sea on

D–9, which is related to the previous cycle of the 10–30-day ISO. This small-scale anticyclonic anomaly moves northward from D–6 and finally merges with the third one (A3) over the Northeast China on D0, strengthening the southern part of A3. The anticyclonic anomaly A3 appears on D–3 and covers the Northeast China and the adjacent region. The combination of A1, A2 and A3 persists from D–3 to D0 and leads to a strong and extensive anticyclonic circulation in the northeastern Asia, concurrent with development of the cyclonic anomaly at about 22°N, 132°E over the western North Pacific. It should be noted here that the cyclonic anomaly coincides with the location of Typhoon In-Fa, and it is possible that the effect of the typhoon could not be totally removed by the 10–30-day bandpass filter. The formation of these anticyclonic and cyclonic anomalies implies that the dipole pattern on D0 could not be simply regarded as a system whose components develop and decay

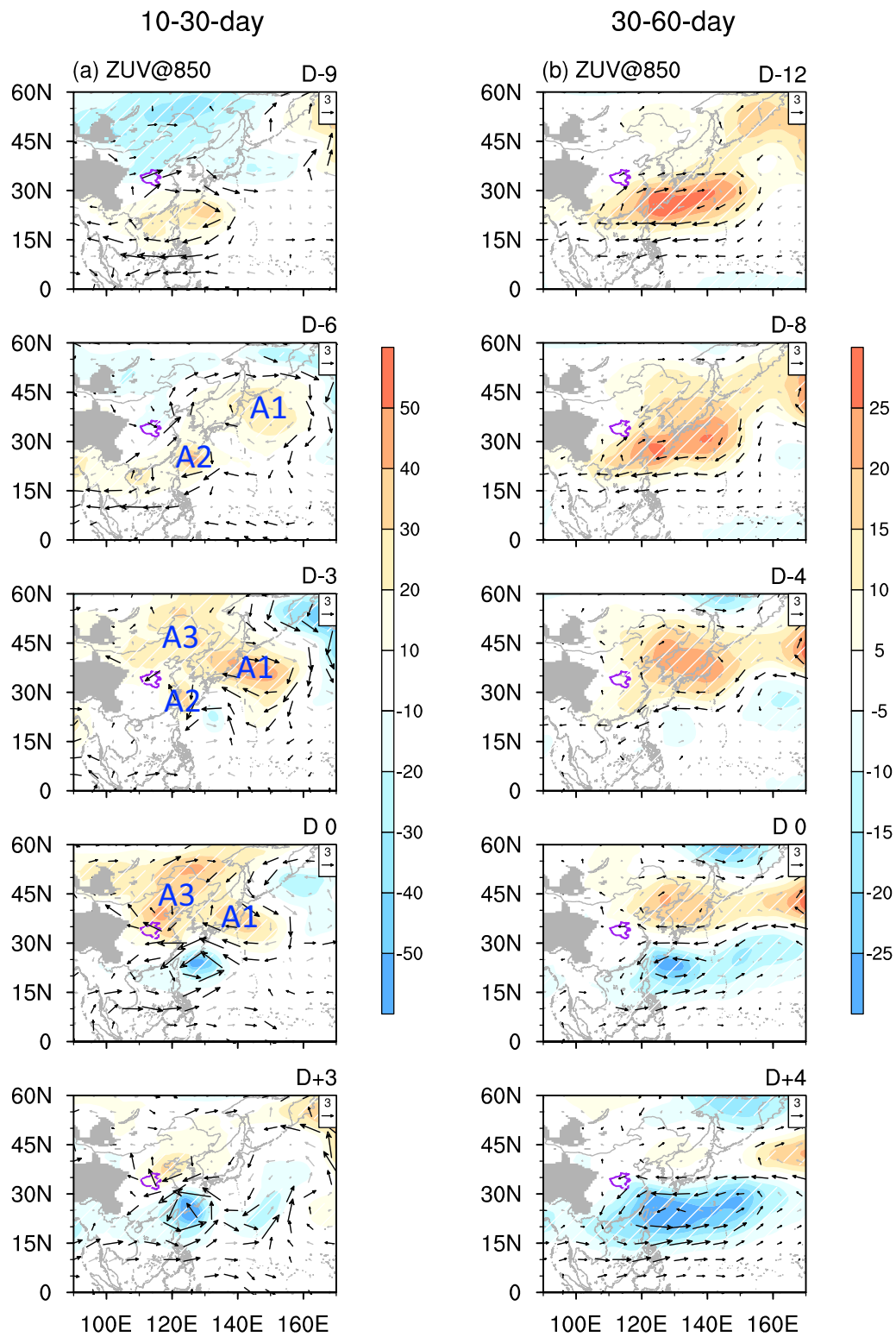


Fig. 3 Lead-lag map of **a** 10–30-day and **b** 30–60-day ISO components of the 850-hPa geopotential height (shaded; gpm) and horizontal winds (vector; m s^{-1}). Henan Province is outlined in purple. The

black vectors and the white oblique lines denote significant at the 90% confidence level. The labels “A1”, “A2” and “A3” represent the anticyclonic anomalies

simultaneously, but it is likely to be influenced by different signals from the tropical and extratropical region.

The 30–60-day filtered atmospheric circulation at the lower level is featured by a noticeable northward propagation. An anticyclonic and high-pressure anomaly dominates the subtropical western North Pacific (about 25°–30°N) on D–12. It then propagates northward and intrudes into the Sea of Japan (about 35°–45°N) on D–4, accompanied by the cyclonic anomaly to its south. As a result, a meridional dipole pattern is discernable over East Asia on D0, strengthening the westward moisture channel southeast to Henan. After that, the anticyclonic anomaly of the dipole pattern decays on D+4, but the cyclonic anomaly continues intensifying and moving northward. The northward-propagating circulation anomalies are reminiscent of the atmospheric circulations associated with the northward-propagating BSISO1, indicating an important role of BSISO1 in the formation of the 30–60-day filtered dipole pattern.

4 Plausible origins of intraseasonal dipole pattern responsible for the extreme rainfall in Henan

4.1 Influences of tropical ISO convections

The evolution of the dipole pattern in both 10–30-day and 30–60-day ISO modes implies the possible influences from the tropical ISOs. In fact, Hsu et al. (2023) has shown significant activities of both BSISO1 and BSISO2 during the extreme rainfall days in Henan through the phase diagram in their Fig. S4. Here we further examine the distribution and evolution of the intraseasonal convective anomalies represented by OLR to illustrate their influences on the intraseasonal dipole pattern (Fig. 4).

For the 10–30-day oscillation (Fig. 4a), the suppressed convection is observed over the tropical western North Pacific and South China Sea on D–9, coherent with the anticyclonic anomaly at the lower troposphere there (Fig. 3a). It is then replaced by the enhanced convection on D–6, albeit less organized. The enhanced convection propagates northwestward and spreads over the western North Pacific on D–3. This northwestward propagation of the enhanced convection as well as the increased rainfall can be seen clearly along the great circle route (blue curve in Fig. 4a) from D–6 (Fig. 5a), reflecting the signal of BSISO2. They can excite a low-level cyclonic anomaly as Rossby wave responses (Gill 1980), which exactly explains the initiation of the cyclonic anomaly on D–3. During this stage, the residual and small-scaled suppressed convection related to the previous ISO cycle can still be observed in East Sea along 120°E, which might contribute to the maintenance of the anticyclonic anomaly A2 (Fig. 3a). Meanwhile,

the suppressed convection is found to be stationary near the Kuroshio Extension region, which might be irrelevant to the northwestward-propagating BSISO2 convection. This suppressed convection appears on D–9, peaks on D–6 and persists to D+3, favoring the transition from the cyclone to anticyclone aloft (Wang et al. 2012) and thus contributing to the formation and duration of the anticyclonic anomaly A1. That is to say, the northwestward-propagating BSISO2 primarily results in the cyclonic anomaly of the dipole pattern but could not directly explain the formation of the anticyclonic anomaly; the latter could be contributed by the local long-lasting suppressed convection, but how this suppressed convection emerges remains to be uncovered.

Convections with a 30–60-day oscillation exhibit a slightly northwest-southeastward-elongated distribution and a salient northward propagation (Figs. 4b and 5b), resembling the common characteristic of the northward-propagating BSISO1 (Lee et al. 2013). These convection anomalies can lead to the emergence of the anticyclonic anomaly over the western North Pacific on D–12 and the cyclonic anomaly on D0 as Rossby wave responses (Gill 1980). We notice that the suppressed convection spreads further north on D–8 and covers the Sea of Japan and the Kuroshio Extension region on D–4 (Fig. 5b), different from the BSISO1 convection that decays when propagating toward the mid-latitude. This suppressed convection persists from D–4 to D+4, leading to the further northward shift of the anticyclonic anomaly (Fig. 3b). However, why the suppressed convection can cross 30°N from the subtropical western North Pacific toward a higher latitude could not be fully explained by the BSISO1 itself; this unusual propagation of BSISO1 convection could be only seen in some cases (Hsu et al. 2017). Considering that the suppressed convection finally arrives in the Kuroshio Extension region where air-sea interactions are active, we speculate that the mid-latitude air-sea interaction would be key to understand the unusual propagation of the intraseasonal convection and will be explored in detail in Sect. 4.3.

4.2 Influences of the mid-latitude wave trains

Both the anomalous anticyclones in the 10–30-day and 30–60-day ISO modes locate in the downstream of the East Asian westerly jet stream. It is reported that the wave train propagating along the westerly wave guide can affect the atmospheric circulation and weather in East Asia (Yang et al. 2010; Li et al. 2021; Guan et al. 2022). To examine whether the mid-latitude wave trains take effects in the anomalous anticyclone over the Northeast Asia, Fig. 6 depicts the evolution of the 200-hPa geopotential height and the WAF anomalies in 10–30-day and 30–60-day ISO modes.

For the 10–30-day ISO mode, the upper-level wave train over the Eurasian Continent is obscure on D–9 but can be

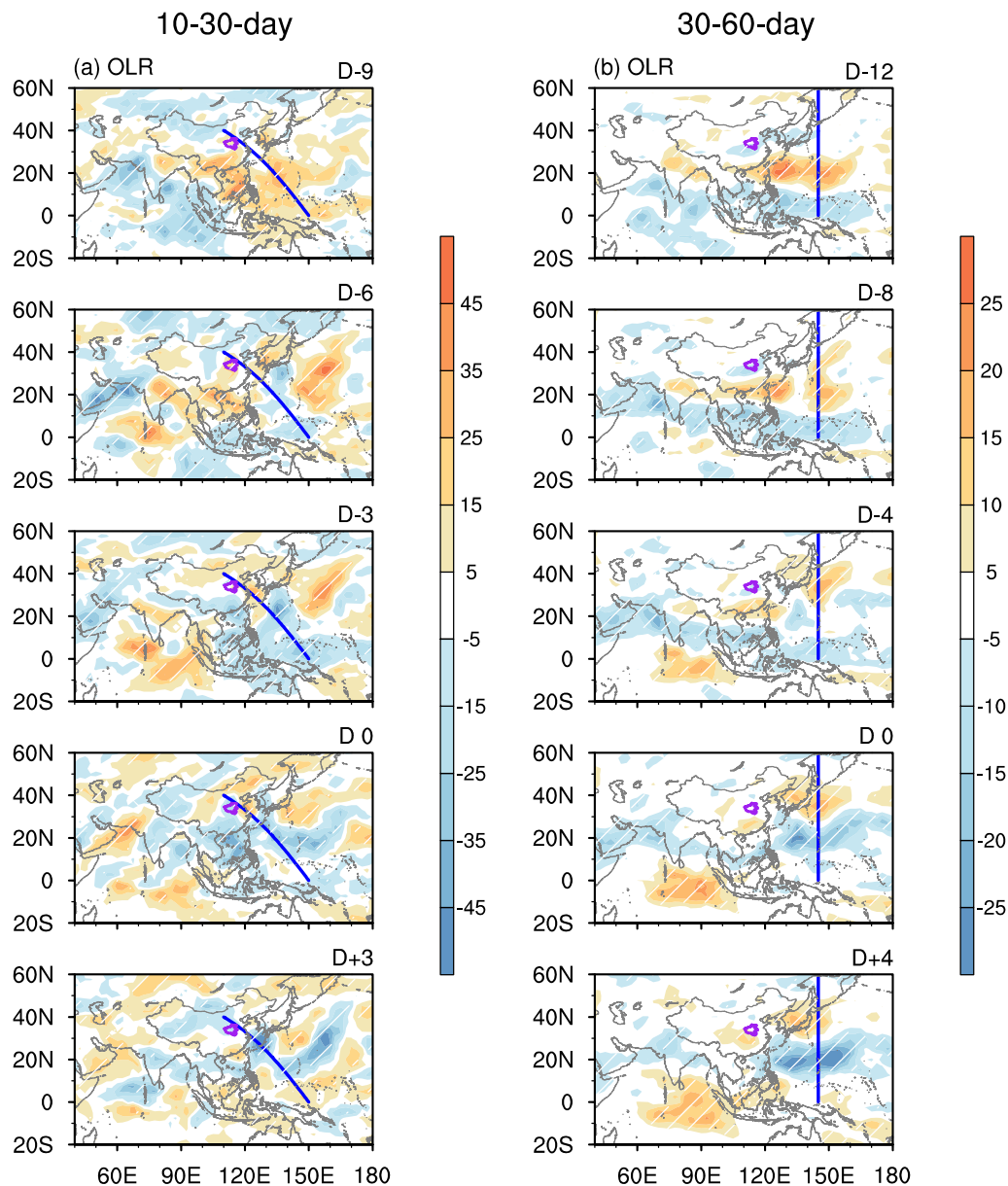


Fig. 4 Same as Fig. 3, but for the OLR (shaded; $W m^{-2}$). The blue curve in **a** denotes the great circle route from $0^\circ, 150^\circ E$ to $40^\circ N, 110^\circ E$. The blue line in **b** denotes the meridional pathway from $0^\circ, 145^\circ E$ to $60^\circ N, 145^\circ E$

clearly identified on D-6 and D-3 (blue curve in Fig. 6a). There are positive centers over the western Europe, the western Mediterranean Sea and the Northeast Asia along $45^\circ N$, accompanied by several negative centers in between (Fig. 6a). The Rossby wave energy disperses eastward, and the eastward propagation can be found in the nodes of the wave train except the negative one east to the Ural Mountain ($\sim 70^\circ E$). Among them, a positive geopotential height anomaly propagates eastward from $80^\circ E$ on D-15 (Fig. 7a). When this positive anomaly ultimately arrives at $120^\circ E$ on D-6, it extends downward to the near surface (Fig. 7b), conducive to the development of the low-level high-pressure

anomaly over the Northeast China (i.e., A3 in Fig. 3a). Meanwhile, another positive geopotential height anomaly originating from $160^\circ W$ propagates westward, encountering the eastward-propagating anomaly around $140^\circ E$ (Fig. 7a). This westward-propagating disturbance may be linked to the mid-latitude ISO over the North Pacific in boreal summer, which propagates westward as well and has a maximum amplitude at $150^\circ W$ (Wang et al. 2013). The disturbance from the east exhibits an equivalent-barotropic structure in the entire troposphere (Fig. 7c), which is directly responsible for the anomalous high-pressure over the Kuroshio Extension region (i.e., A1 in Fig. 4a) along with the influence of

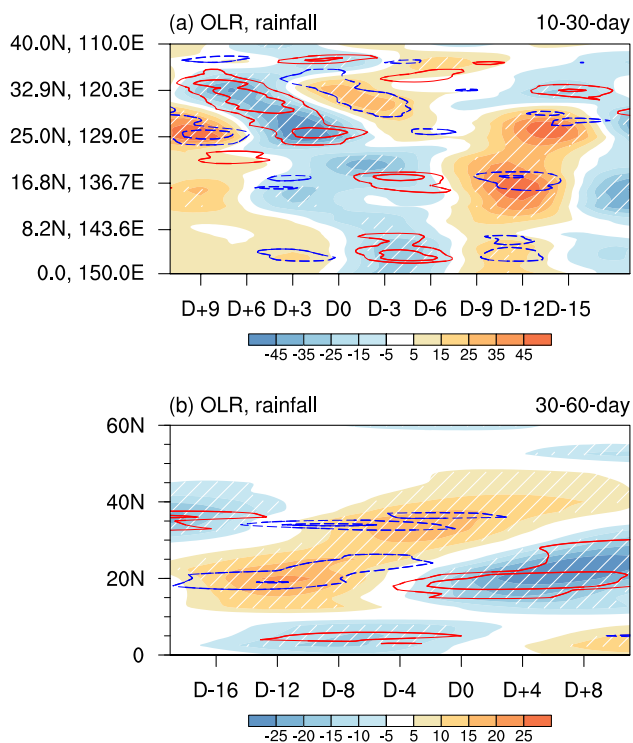


Fig. 5 Hovmöller diagram of **a** the 10–30-day filtered OLR (shaded; W m^{-2}) and rainfall (contour; mm day^{-1}) along the great circle route from 0° , 150°E to 40°N , 110°E (blue curve in Fig. 4a) and the 30–60-day filtered OLR along 145°E from 0° to 60°N . The contours represent -20 , -10 , 10 , and 20 mm day^{-1} in **a** and -8 , -4 , 4 , and 8 mm day^{-1} in **b**. Contours in red indicate the positive anomaly and in blue the negative anomaly. The white oblique and thick curve denote significant at the 90% confidence level

the local suppressed convection (Fig. 4a). It suggests that the internal forcings from both upstream and downstream in the mid-latitude region contribute to the northern node of the 10–30-day filtered dipole pattern. On D0, another wave train develops along 60°N , and the positive geopotential height anomaly over the Northeast Asia moves northwestward, having little influence on the duration of the high-pressure anomaly at the lower level.

The significant signals mainly appear in the high-latitude region (north to 60°N) on D – 12 for the 30–60-day ISO mode. There is a strong negative geopotential height anomaly over northern Eurasian continent and positive anomaly over the northern Europe and the eastern Russia, with the WAF propagating eastward (Fig. 6b). On D – 8, weak Rossby wave energy is found propagating southward from the negative center, which may favor the development of the high-pressure anomaly over the Northeast China. Subsequently, this high-pressure anomaly gets intensified and persists from D – 4 to D + 4. At the meantime, the negative anomaly over the subtropical western North Pacific strengthens along 30°N , which may be contributed by the southeastward WAF from the positive anomaly to the north. To explore how these

upper-level signals affect those at the lower level, Fig. 8 displays the vertical profile of the geopotential height and wind anomalies averaged along 130° – 140°E . It is found that the positive anomaly extends the entire troposphere from 20°N to 55°N and exhibits a northward-tilted structure on D – 12 (Fig. 8a). The strengthened upper-level high-pressure anomaly is associated with the convergence anomaly (dashed contour in Fig. 8) to its south on D – 8, which further induces the anomalous descending motion at about 40°N (Fig. 8b). The anomalous downward flow helps the development of the anticyclonic anomaly at the lower level, leading the vertical structure of the positive anomaly to be barotropic on D0 (Fig. 8c–d). Similarly, the strengthening of the upper-level negative anomaly between 20° – 30°N causes the upward motion anomaly to its south, which is conducive to the development of the low-level low-pressure anomaly.

4.3 Influences of the SST anomaly over Sea of Japan and Kuroshio Extension region

Figure 4 has already shown the suppressed convection over the Sea of Japan and Kuroshio Extension region responsible for the anticyclonic anomaly aloft in both 10–30-day and 30–60-day ISO modes, but how the suppressed convection develops needs to be uncovered. We suppose that the forcing from the underlying ocean surface may play a role because active air-sea interactions on the intraseasonal time scale occur in the boreal summer over the Kuroshio Extension region where the suppressed convection locates (Wang et al. 2012; Takahashi and Hayasaka 2020). Changes of the SST anomalies in both 10–30-day and 30–60-day ISO modes are thus detected in Fig. 9. It can be clearly found that cold SST anomalies dominate the Sea of Japan and Kuroshio Extension region a week before D0. They then fade out, followed by the warm SST anomaly after D0. The intraseasonal suppressed convection develops during the cold-to-warm transition of SST anomaly (Figs. 4 and 9), implying a possible role of the ocean forcing upon the atmosphere.

How does the preceding cold SST anomaly drive the change of the convection anomaly? Fig. 10 presents the evolution of the relevant variables over the Sea of Japan and Kuroshio Extension region (35° – 45°N , 130° – 160°E). For the 10–30-day ISO mode, the coldest SST anomaly appears on D – 9. It inhibits the upward latent heat flux (Fig. 10c) via decreasing humidity contrast between surface and near-surface air, accompanied by the decelerated near-surface wind (Fig. S2a), indicating the diabatic cooling near the surface. This diabatic cooling contributes to the cooler air at the lower level than the aloft (Fig. S2c), causing the reduction of the convective instability represented by the difference of equivalent potential temperature between 1000 and 850 hPa (Fig. 10c). As a result, the cooling of the ocean surface over the Kuroshio Extension region leads to a more

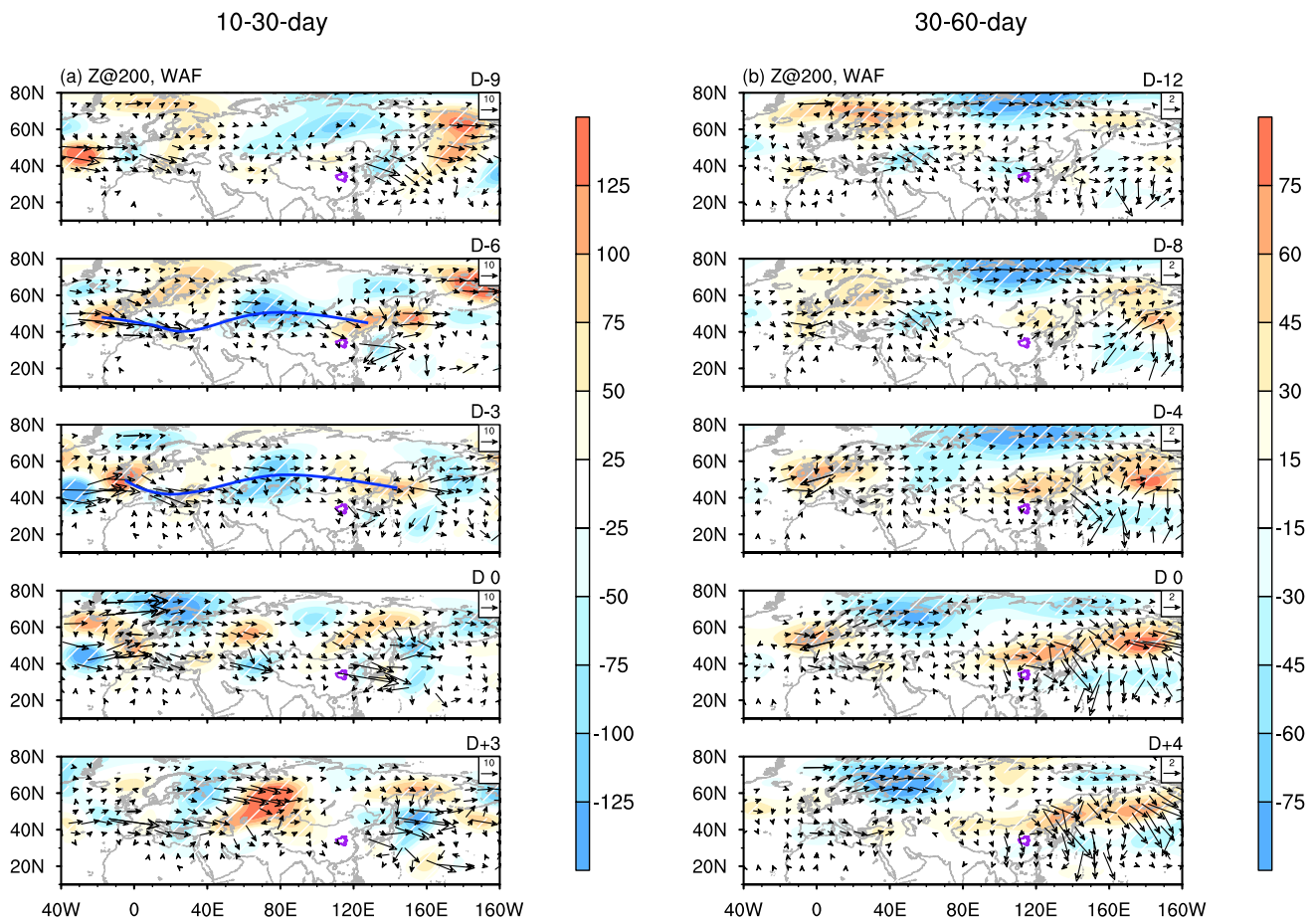


Fig. 6 Same as Fig. 3, but for the 200-hPa geopotential height (shaded; gpm) and wave activity flux (WAF) (vector; $m^2 s^{-2}$). Only the fluxes greater than $1 m^2 s^{-2}$ are shown as vectors. The blue curve represents the general location of mid-latitude wave train

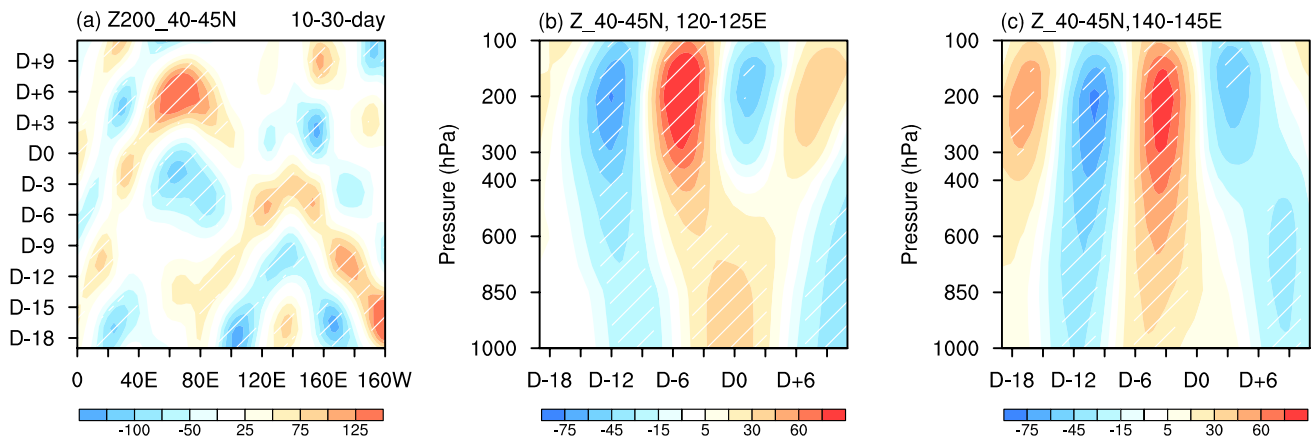


Fig. 7 a Longitude-time cross section of the 10–30-day filtered geopotential height anomaly at 200-hPa averaged along 40°–45°N. Time-level cross section of 10–30-day filter geopotential height

anomaly averaged over **b** 40°–45°N, 120°–125°E and **c** 40°–45°N, 140°–145°E. The white oblique lines denote significant at the 90% confidence level

stable atmosphere, which is hostile to the rainfall (Fig. 10e) and convective activity (Fig. 4a). The suppressed convection further favors the transition from the cyclone to anticyclone

aloft, in line with Wang et al. (2012). As the upper-level anticyclonic anomaly moves northwestward after D–3, the long-lasting suppressed convection primarily maintains the

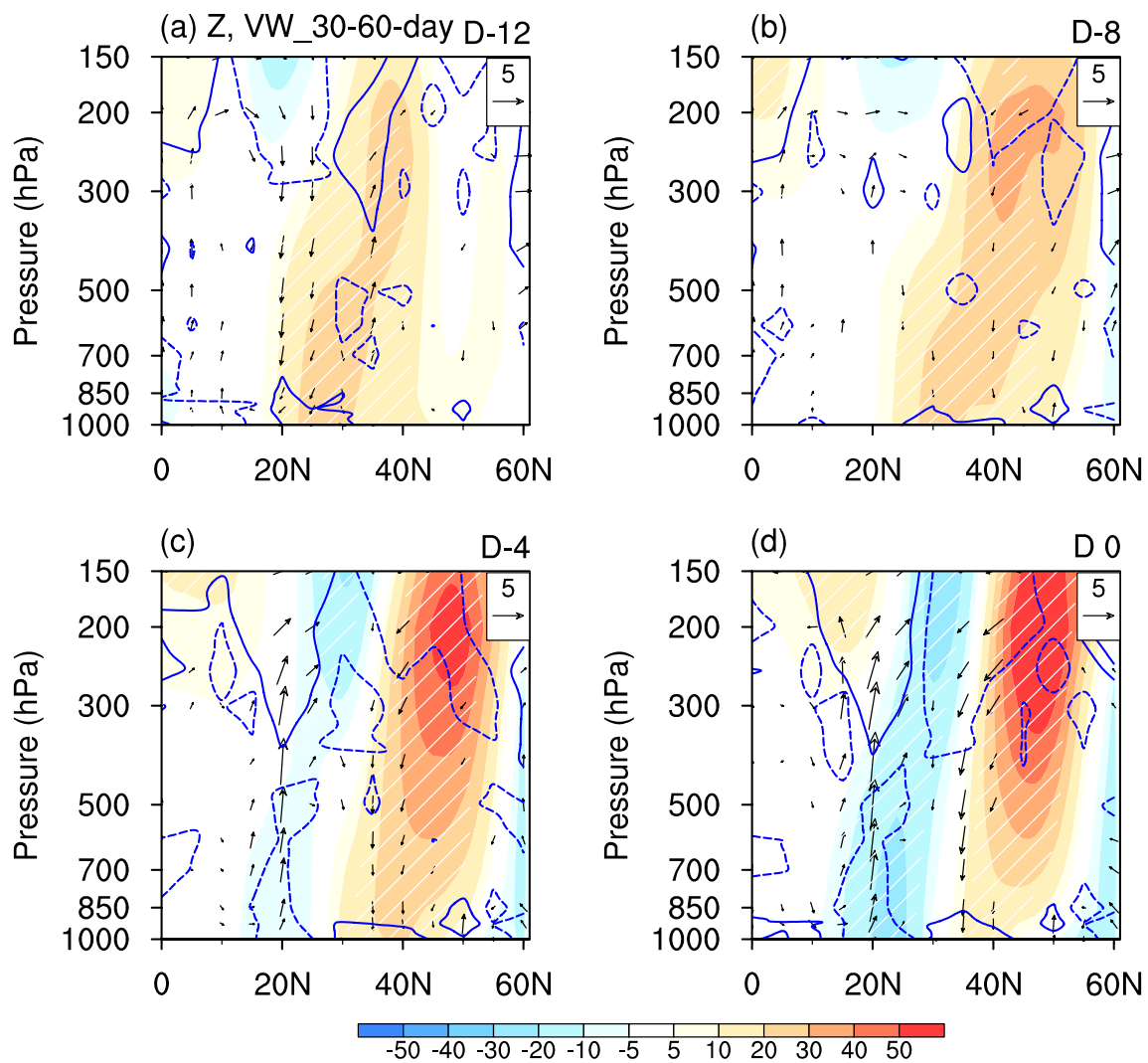


Fig. 8 Lead-lag map of 30–60-day ISO components of the geopotential height (shaded; gpm) and meridional-vertical section of winds (vector; m s^{-1} for meridional wind and $10^{-2} \text{ Pa s}^{-1}$ for vertical velocity at p coordinates) averaged along 130° – 140°E on **a** D–12, **b** D–8, **c** D–4 and **d** D0. The white oblique lines and black vec-

tors denote significant at the 90% confidence level. The blue solid and dashed contours represent the anomalous divergence (greater than $5 \times 10^{-7} \text{ s}^{-1}$) and convergence zones (less than $-5 \times 10^{-7} \text{ s}^{-1}$), respectively

anticyclonic anomaly. This anticyclonic anomaly would be conducive to the descending and the less cloudiness could increase the downward solar radiation (Fig. 10a), which in turn causes a negative feedback on the SST anomaly as suggested by (Wu and Kinter 2010).

Similar physical processes exist in the 30–60-day ISO mode (Fig. 10b, d, f). The cooling over the Sea of Japan and Kuroshio Extension region on D–12 would inhibit the rainfall and convective activity via stabilizing the atmosphere, leading to the anticyclonic anomaly. Briefly speaking, in addition to the tropical ISOs and mid-to-high latitude wave trains, the preceding cold SST would also be the contributor to the development and maintenance of the anticyclonic anomaly in both 10–30-day and 30–60-day ISO modes,

which could not be ignored when considering the attribution of the extreme rainfall in Henan.

One intriguing phenomenon mentioned above is the intimate relationship between the BSISO1 and mid-latitude SST anomaly in July 2021, which is less understood before. Considering that the suppressed convection exhibits a consecutive poleward propagation from the tropical western Pacific, the mid-latitude SST anomaly could be regarded as an intermediate forcing that pushes the anomalous BSISO1 convection to a further north latitude. Is this relationship found frequently in the past several decades or occasionally in July 2021? We attempt to answer it by analyzing the northward propagation feature of the 30–60-day filtered tropical convections. The suppressed convection

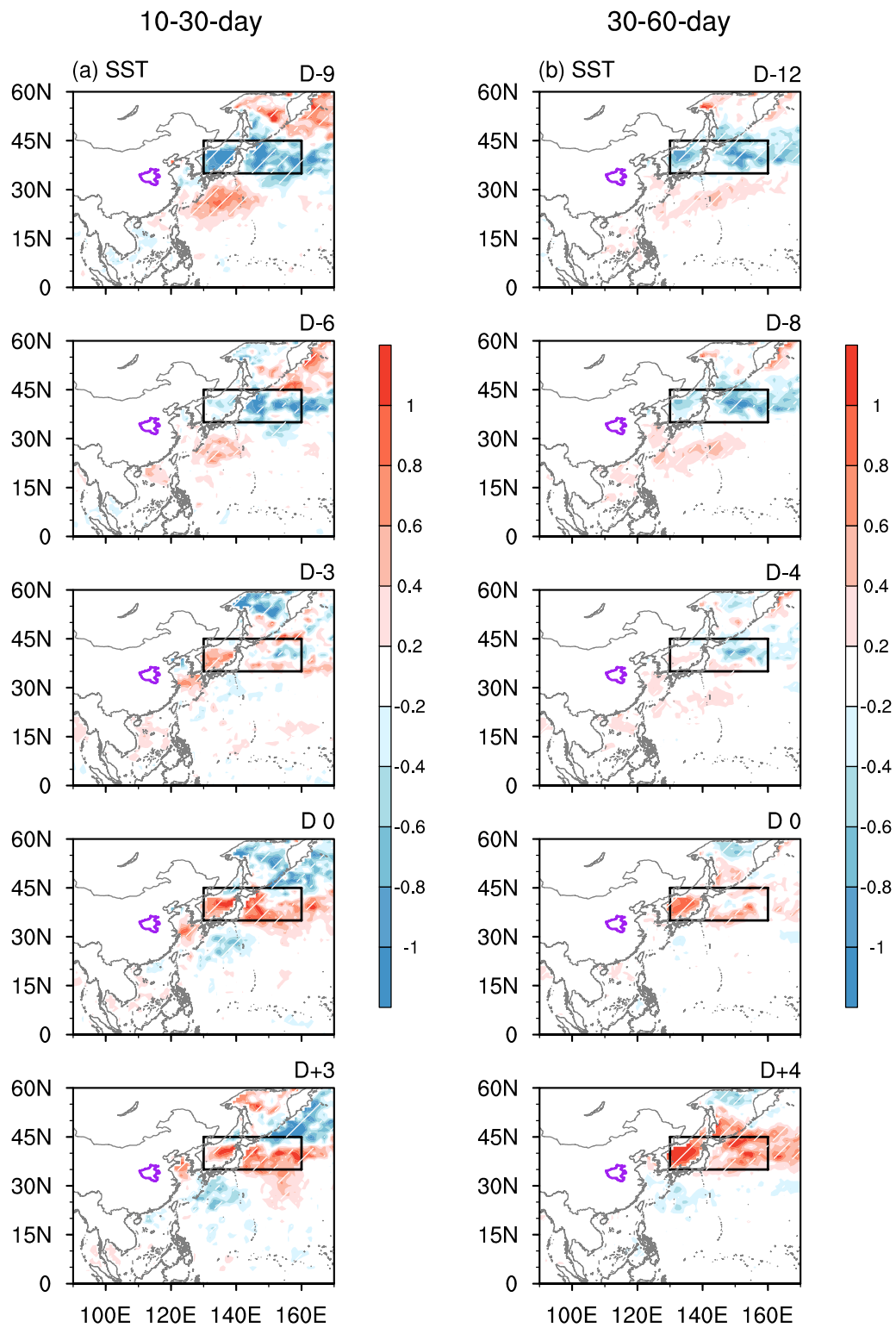


Fig. 9 Same as Fig. 3, but for SST anomaly (shaded; °C). The black rectangle denotes the region of 35°–45°N, 130°–160°E

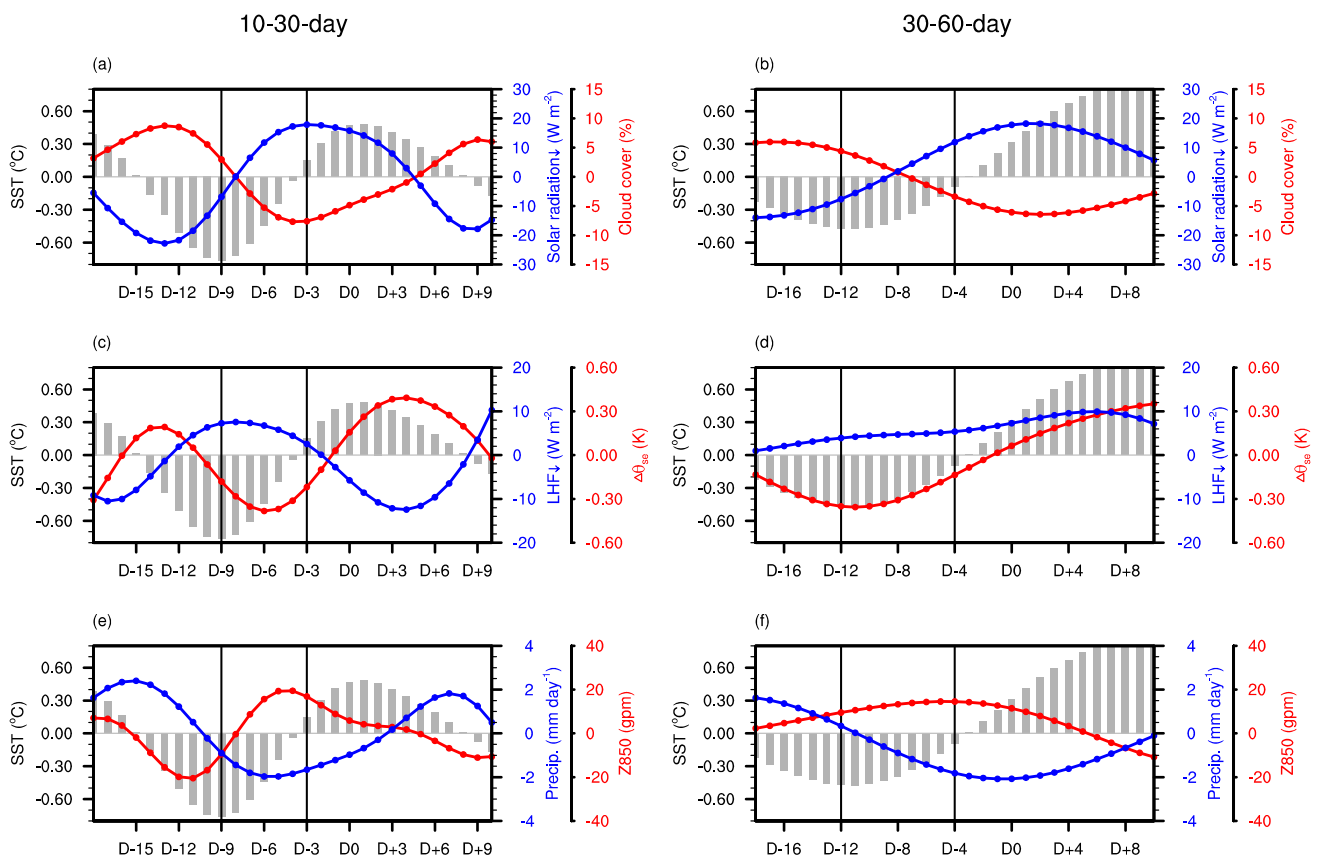


Fig. 10 Time series of **a, b** downward solar radiation (blue; $W m^{-2}$) and cloud cover (red; %), **c, d** downward surface latent heat flux (blue; $W m^{-2}$) and convective instability (red; K), and **e, f** total precipitation (blue; $mm day^{-1}$) and geopotential height at 850 hPa (red;

gpm) averaged over 35° – $45^{\circ}N$, 130° – $160^{\circ}E$ in the 10–30-day (left panel) and 30–60-day ISO modes (right panel). The SST anomaly ($^{\circ}C$) is shown as gray bar

events are first defined based on the 30–60-day filtered OLR anomaly over the western North Pacific (15° – $25^{\circ}N$, 130° – $160^{\circ}E$) from May to October. A common-propagating dry event is identified if the area-averaged OLR is above 1 standard deviation for at least five successive days, and the day when the OLR reaches its maximum is referred to as D0 here. Then an unusual-propagating dry event is selected if the OLR anomaly propagates northward continuously and reaches at least $35^{\circ}N$ based on the time-latitude cross sector (Hovmöller diagram) along 130° – $160^{\circ}E$. There are 95 common-propagating dry events, while only 8 dry events with convections propagating further north are found (Fig. S3). Their composite diagrams based on D0 are used for comparison.

It is found that the suppressed convection originating from the tropics can reach nearly $40^{\circ}N$ in the unusual-propagating dry event (Fig. 11d), while it generally stops at $30^{\circ}N$ in the common-propagating dry event (Fig. 11c). Moreover, before the dry signal arrives at the mid-latitude region in the unusual-propagating event, the cold SST anomaly ($\sim 0.10^{\circ}C$) is observed over the Sea of Japan and Kuroshio Extension

region (Fig. 11b). As a comparison, the SST anomaly is feeble ($\sim 0.02^{\circ}C$) for the common-propagating dry events (Fig. 11a), which may inhibit the convection anomaly to move off the subtropical region. In this case, the most evident SST anomaly is primarily confined to the subtropical western North Pacific (Fig. S4). Statistically, the probability of the further northward-propagation convection anomaly coupled by the mid-latitude SST anomaly is merely 7.8% among all the propagating dry events. It suggests that the further northward propagation of tropical intraseasonal convections is not a common feature but would occur in cooperation with the mid-latitude SST anomaly, which can partly explain the unprecedented nature of the Henan rainfall event in July 2021. It also provides an opportunity for the BSISO1 to extend its influence from the monsoon onset (e.g., Yasunari 1980, 1981) and active/break cycle (e.g., Krishnamurti and Bhalme 1976; Annamalai and Sperber 2005), East Asian summer rainfall and heatwave (e.g., Hsu et al. 2016, 2017), to the atmospheric circulations over the mid-latitude region. Thus the BSISO1’s influence on the mid-latitude region would be more direct rather than through

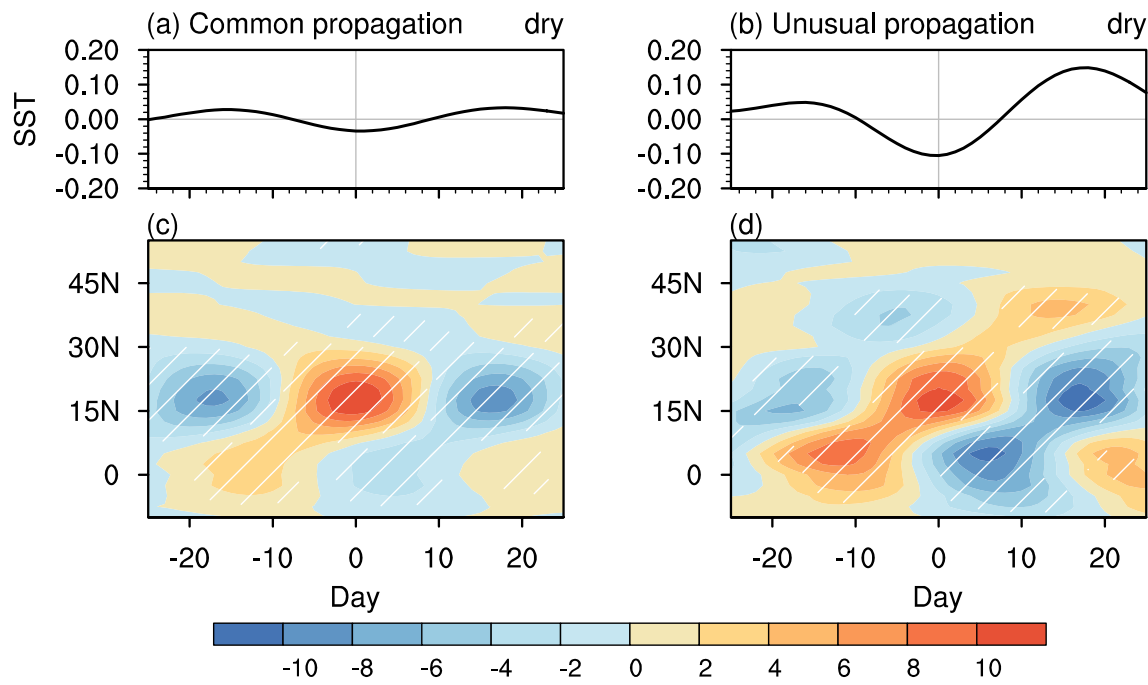


Fig. 11 **a,b** Evolution of composite SST anomaly averaged over 35°–45°N, 130°–160°E and **c,d** Hovmöller diagram of composite OLR averaged along 130°–160°E in common-propagating dry events (left

panel) and unusual-propagating dry events (right panel) in the 30–60-day ISO mode. The white oblique lines denote the 90% confidence level based on the two-tailed Student's *t*-test

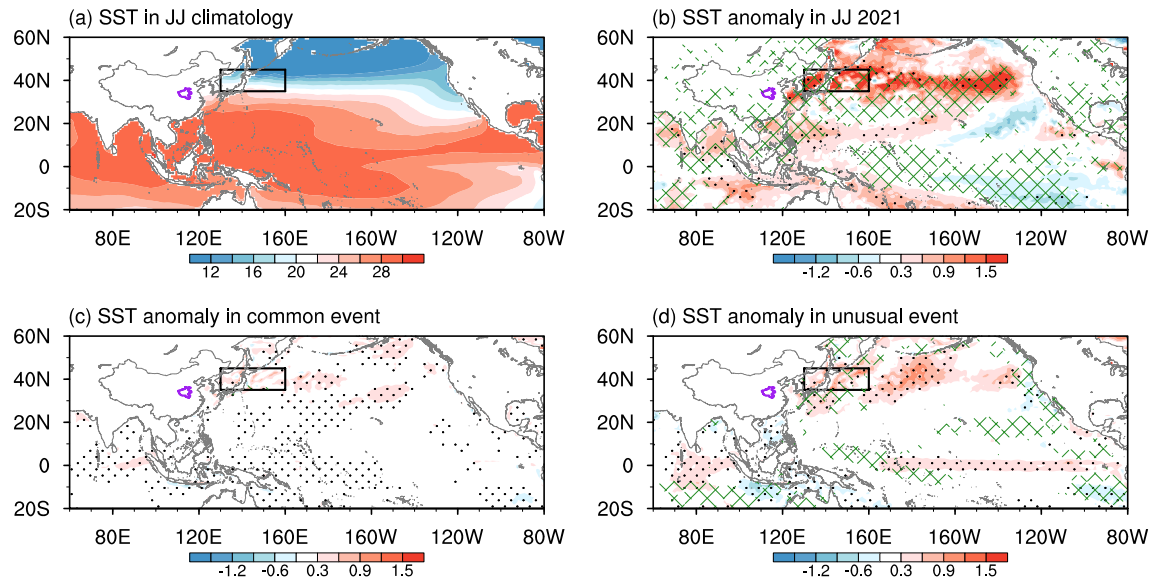


Fig. 12 **a** Climatological SST (shaded; °C) averaged from June to July. Anomalous SST (shaded; °C) averaged **b** from June to July in 2021, **c** from D–30 to D+30 in common-propagating events and **d** in unusual-propagating events. The green cross represents the surface

upward latent heat flux greater than 5 W m⁻². The black dots denote significant at the 90% confidence level. The black rectangle indicates the region of 35°–45°N, 130°–160°E

the teleconnection excited by the convection anomaly in the tropical region (Moon et al. 2013).

The next question emerges that what drives the active air-sea interaction in the Sea of Japan and Kuroshio

Extension region in July 2021? On the one hand, the cold SST anomaly could be traced back to the incipient cloudiness and the reduction of the shortwave radiation induced by the increased rainfall anomaly from the perspective of

intraseasonal time scale, indicating an active air-sea interaction there (Fig. 11a). On the other hand, we found that during June and July in 2021, an anomalously zonal warming belt is observed from west to east of the mid-latitude North Pacific where strong meridional SST gradients locate (Fig. 12a, b). This warm SST anomaly is accompanied by the increased surface upward latent heat flux anomaly, which may provide a favorable condition to perturb the atmosphere and the SST anomaly. A similar warming mean state could be found in the mid-latitude North Pacific when the unusual-propagating event occurs, though the amplitude is weaker than that in 2021 (Fig. 12d); but the warm SST anomaly over the Sea of Japan and Kuroshio Extension region is much subtle in the common-propagating event (Fig. 12c). It confirms that under a warmer mean state in the mid-latitude North Pacific, if active convective activities in the subtropical western North Pacific happens to be concurrent with the SST anomaly over the Sea of Japan and Kuroshio Extension region, the convection would be likely pushed further north, directly affecting the atmospheric circulation in the mid-latitude region.

5 Summary and discussion

Previous research has paid much attention to the underlying mechanism whereby the large-scale condition and the mesoscale convective system affect the Henan extreme rainfall event (e.g., Ran et al. 2021; Liang et al. 2022; Yin et al. 2022), but few has a deeper investigation on the origin of the related atmospheric circulations. The present study tries to fill this gap from a perspective of the intraseasonal time scale. It is found that the Henan extreme rainfall is featured by the 10–30-day and 30–60-day ISOs. These two ISOs contribute more than half (~52%) of the total rainfall from 17 to 22 July, with the 10–30-day ISO mode (~37%) being

larger than the 30–60-day ISO mode (~15%). The related atmospheric circulations exhibit a meridional dipole pattern, characterized by a cyclonic circulation over the western North Pacific and an anticyclonic circulation covering the Northeast China, Sea of Japan and Kuroshio Extension region. The strong easterly anomalies in between the cyclonic and anticyclonic anomalies are key for abundant moisture transport from ocean and moisture convergence in the central-northern Henan, which directly gives rise to the extreme rainfall therein. These intraseasonal patterns are generally consistent with those in Hsu et al. (2023) who demonstrated that the interaction between the ISO flow and increased moisture background is important for the extreme rainfall in Henan. We extended their work by investigating how the ISO flows originate by exploring the influence of the tropical and extratropical forcings, which can provide potential precursors for the extreme rainfall event in Henan.

Figure 13 gives a schematic diagram of the relevant physical processes contributing to the dipole pattern in 10–30-day and 30–60-day ISO modes. In general, they are in part attributed to the tropical ISO convections and the mid-to-high latitude wave trains. In the 10–30-day ISO mode (Fig. 13a), the cyclonic anomaly is primarily induced by the northwestward propagating BSISO2 convection, while the anticyclonic anomaly is driven by the joint influence of the mid-latitude Rossby wave train that propagates eastward and westward as well as the northward shift of a small-scale anticyclonic anomaly related to the previous ISO cycle. The 30–60-day filtered dipole pattern (Fig. 13b) is mainly caused by the BSISO1 convection, which could directly excite the low-level cyclonic and anticyclonic anomalies as Rossby wave response. It is then enhanced by the upper-level mid-to-high latitude wave train through anomalous vertical motions.

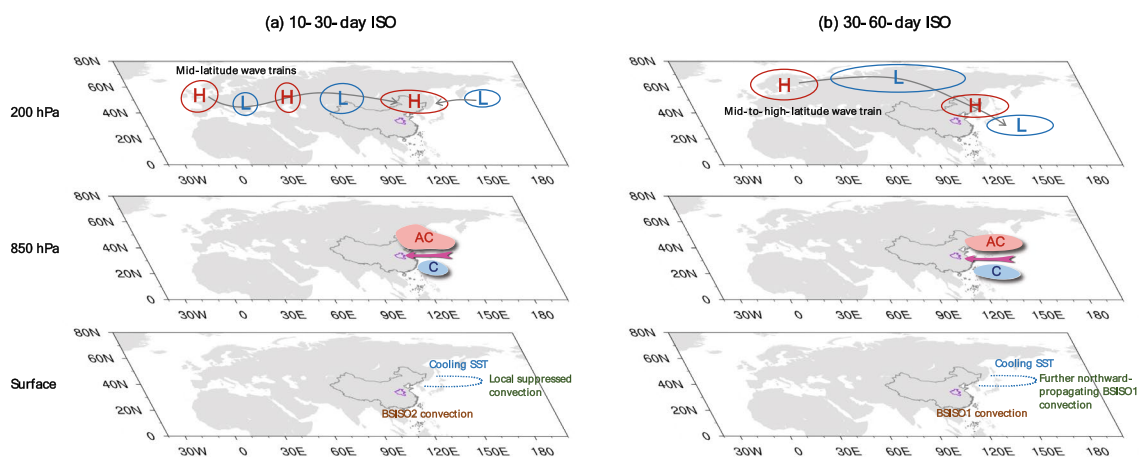


Fig. 13 Schematic diagram of the physical processes whereby **a** the 10–30-day and the **b** 30–60-day filtered tropical and extratropical forcings contribute to the meridional dipole pattern and the extreme rainfall event in Henan in July 2021

In addition, we highlight that the mid-latitude SST anomaly is also the potential source for the ISO circulations responsible for the extreme rainfall in Henan, which should not be ignored for the subseasonal prediction of the extreme weather. The cooling SST anomaly is found over the Sea of Japan and Kuroshio Extension region, prior to the anomalous anticyclone of the dipole pattern. This SST cooling could lead to a more stable atmosphere via influencing the latent heat flux and the temperature difference between the surface and low-level atmosphere, causing suppressed convection and finally the development of the anticyclonic anomaly in situ. The anticyclonic high-pressure anomaly in turn exerts negative feedback on the SST anomaly through less cloudiness and increased solar radiation, indicating an active role of the mid-latitude air-sea interaction. In the 10–30-day ISO mode, this cold SST-suppressed convection relationship occurs locally, directly conducive to the duration of the anticyclonic anomaly. In the 30–60-day ISO mode, the above-mentioned SST cold anomaly could stimulate the BSISO1 convection to propagate further north and invade the mid-latitude region, contributing to the anomalous anticyclone there. The concurrent relationship between the northward-propagating BSISO1 and mid-latitude air-sea interaction is rarely found from 1979 to 2020, as the occurrence probability is only 7.8% among all events with the suppressed convection appearing over the subtropical western North Pacific. Moreover, this unique phenomenon tends to occur under the warmer SST background condition and the attendant increased upward latent heat flux, implying a modulation of the SST mean state on the intraseasonal variability.

The influence of the transient eddy feedback could not be ignored when considering the mid-latitude dynamics. Wang et al. (2012) pointed out that on the intraseasonal time scale, the atmospheric circulation anomaly response to the heating induced by the SST anomaly tends to be baroclinic at first, and then it would change to a barotropic vertical structure due to the transient eddy activities. We found the extended E-P flux representing the transient eddy activities converging in the entire troposphere from D–7, concurrent with the anomalously strong easterly in the southern flank of the anticyclonic anomaly at the upper level (Fig. S5). It reflects a contribution of the frequent transient eddy activity to the weakened westerly mean flow and explains the barotropic vertical structure of the dipole pattern.

By far, it is still unclear how these mid-to-high latitude wave trains originate. The wave trains over the Eurasian continent could be traced back to the cyclonic/anticyclonic anomaly over the North Atlantic (Fig. 6). Li et al. (2021) found that during the persistent severe flood over the Yangtze River basin, strong barotropic energy conversion from the mean flow to intraseasonal flows could excite strong ISO signal over the North Atlantic. However, Du and Lu

(2021) demonstrated that the intraseasonal wave train over the North Pacific is maintained by the baroclinic energy conversion associated with the vertical shear of the westerly mean state. More research is needed to understand the atmospheric internal processes contributing to the intraseasonal wave trains in July 2021. In addition, similar patterns of these wave trains can be seen in the July-mean result as shown by Liu et al. (2023). They revealed that the mid-latitude wave train in July 2021 is triggered by the record-high warm Atlantic Ocean and the cyclonic anomaly in the Arctic polar region is induced by the sea-ice loss over the Laptev-East Siberian Seas. Their results can give a hint to further understand the impact of the external forcing on the mid-to-high latitude atmospheric circulation anomalies responsible for the extreme rainfall in Henan. Since the length of one month is between the 10–30-day and 30–60-day oscillation, whether the Atlantic SST and the polar sea-ice exhibit a similar intraseasonal variability in the summer of 2021 and change the atmosphere correspondingly deserves further investigations.

Supplementary Information The online version contains supplementary material available at <https://doi.org/10.1007/s00382-023-07052-7>.

Acknowledgements This research is supported by the National Natural Science Foundation of China (42105017 and 42205019). S. Huang is supported by China Postdoctoral Science Foundation (2022M710715).

Funding This research was supported by the National Natural Foundation No. 42105017 and 42205019. S. Huang has received research support from China Postdoctoral Science Foundation (2022M710715).

Data availability The observed rainfall record of national stations in Henan Province could be downloaded from China Meteorological Data Service Centre (<http://data.cma.cn/en/?r=site/index>). The reanalysis data from ERA5 was derived from <https://cds.climate.copernicus.eu/cdsapp#!/dataset/>. The OLR and SST data is downloaded from https://www.psl.noaa.gov/data/gridded/data.interp_OLR.html and <https://www.psl.noaa.gov/data/gridded/data.noaa.oisst.v2.highres.html>, respectively.

Declarations

Conflict of interest The authors have no relevant financial or non-financial interests to disclose.

References

- Annamalai H, Slingo JM (2001) Active/break cycles: diagnosis of the intraseasonal variability of the Asian Summer Monsoon. *Clim Dyn* 18:85–102
- Annamalai H, Sperber KR (2005) Regional Heat Sources and the Active and Break Phases of Boreal Summer Intraseasonal (30–50 Day) Variability. *J Atmos Sci* 62:2726–2748. <https://doi.org/10.1175/jas3504.1>
- Chen Y, Zhai P (2017) Simultaneous modulations of precipitation and temperature extremes in Southern parts of China by the boreal

- summer intraseasonal oscillation. *Clim Dyn* 49:3363–3381. <https://doi.org/10.1007/s00382-016-3518-4>
- Ding Y (2015) On the study of the unprecedented heavy rainfall in Henan province during 4–8 august 1975: reviews and assessment. *Acta Meteorol Sin* 73:411–424. <https://doi.org/10.11676/qxxb2015.067>
- Ding Q, Wang B (2007) Intraseasonal teleconnection between the summer Eurasian wave train and the Indian Monsoon. *J Clim* 20:3751–3767. <https://doi.org/10.1175/JCLI4221.1>
- Du L, Lu R (2021) Wave trains of 10–30-day meridional wind variations over the north pacific during summer. *J Clim* 34:9267–9277. <https://doi.org/10.1175/JCLI-D-21-0096.1>
- Duchon CE (1979) Lanczos filtering in one and two dimensions. *J Appl Meteorol* 18:1016–1022
- Fu SM, Yu F, Wang DH, Di XR (2013) A comparison of two kinds of eastward-moving mesoscale vortices during the mei-yu period of 2010. *Sci China Earth Sci* 56:282–300. <https://doi.org/10.1007/s11430-012-4420-5>
- Gao Y, Hsu P-C, Che S et al (2022) Origins of intraseasonal precipitation variability over North China in the rainy season. *J Clim* 35:6219–6236. <https://doi.org/10.1175/jcli-d-21-0832.1>
- Gill AE (1980) Some simple solutions for heat induced tropical circulation. *Q J R Meteorol Soc* 106:447–462. <https://doi.org/10.1002/qj.49710644905>
- Guan X, Gao J, Li T et al (2022) Multiscale influences on persistent extreme precipitation events in North China. *Front Earth Sci* 10:1–15. <https://doi.org/10.3389/feart.2022.893152>
- Hersbach H, Bell B, Berrisford P et al (2020) The ERA5 global reanalysis. *Q J R Meteorol Soc* 146:1999–2049. <https://doi.org/10.1002/qj.3803>
- Hsu PC, Lee JY, Ha KJ (2016) Influence of boreal summer intraseasonal oscillation on rainfall extremes in southern China. *Int J Climatol* 36:1403–1412. <https://doi.org/10.1002/joc.4433>
- Hsu PC, Lee JY, Ha KJ, Tsou CH (2017) Influences of boreal summer intraseasonal oscillation on heat waves in monsoon asia. *J Clim* 30:7191–7211. <https://doi.org/10.1175/JCLI-D-16-0505.1>
- Hsu PC, Xie J, Lee JY et al (2023) Multiscale interactions driving the devastating floods in Henan Province, China during July 2021. *Weather Clim Extrem* 39:100541. <https://doi.org/10.1016/j.wace.2022.100541>
- Hu S, Zhou T, Wu B, Chen X (2023) Seasonal prediction of the record-breaking northward shift of the Western Pacific subtropical high in July 2021. *Adv Atmos Sci* 40:410–427. <https://doi.org/10.1007/s00376-022-2151-x>
- Huang S, Wen Z, Chen X et al (2022) The Henan extreme rainfall in July 2021: modulation of the northward-shift monsoon trough on the synoptic-scale wave train. *Adv Clim Chang Res* 13:819–825. <https://doi.org/10.1016/j.accre.2022.11.001>
- IPCC (2021) *Climate Change 2021: The Physical Science Basis. Contribution of Working Group I to the Sixth Assessment Report of the Intergovernmental Panel on Climate Change* [Masson-Delmotte, V., P. Zhai, A. Pirani, S.L. Connors, C. Péan, S. Berger, N. Caud, Y. Chen,
- Kemball-Cook S, Wang B (2001) Equatorial waves and air-sea interaction in the boreal summer intraseasonal oscillation. *J Clim* 14:2923–2942. [https://doi.org/10.1175/1520-0442\(2001\)014%3c2923:EWAASI%3e2.0.CO;2](https://doi.org/10.1175/1520-0442(2001)014%3c2923:EWAASI%3e2.0.CO;2)
- Krishnamurti TN, Bhalme HN (1976) Oscillations of a monsoon system. Part I. Observational Aspect *J Atmos Sci* 33:1937–1954. [https://doi.org/10.1175/1520-0469\(1976\)033%3c1937:OOAMSP%3e2.0.CO;2](https://doi.org/10.1175/1520-0469(1976)033%3c1937:OOAMSP%3e2.0.CO;2)
- Lee JY, Wang B, Wheeler MC et al (2013) Real-time multivariate indices for the boreal summer intraseasonal oscillation over the Asian summer monsoon region. *Clim Dyn* 40:493–509. <https://doi.org/10.1007/s00382-012-1544-4>
- Li J, Mao J (2018) The impact of interactions between tropical and midlatitude intraseasonal oscillations around the Tibetan plateau on the 1998 Yangtze floods. *Q J R Meteorol Soc* 144:1123–1139. <https://doi.org/10.1002/qj.3279>
- Li J, Mao J (2019a) Impact of the boreal summer 30–60-day intraseasonal oscillation over the asian summer monsoon region on persistent extreme rainfall over Eastern China. *Chinese J Atmos Sci* 43:796–812. <https://doi.org/10.3878/j.issn.1006-9895.1809.18145>
- Li J, Mao J (2019b) Coordinated influences of the tropical and extratropical intraseasonal oscillations on the 10–30-day variability of the summer rainfall over southeastern China. *Clim Dyn* 53:137–153. <https://doi.org/10.1007/s00382-018-4574-8>
- Li J, Mao J, Wu G (2015) A case study of the impact of boreal summer intraseasonal oscillations on yangtze rainfall. *Clim Dyn* 44:2683–2702. <https://doi.org/10.1007/s00382-014-2425-9>
- Li J, Zhai P, Mao J et al (2021) Synergistic effect of the 25–60-day tropical and midlatitude intraseasonal oscillations on the persistently severe yangtze floods. *Geophys Res Lett* 48:1–9. <https://doi.org/10.1029/2021GL095129>
- Liang X, Xia R, Bao X et al (2022) Preliminary investigation on the extreme rainfall event during July 2021 in Henan Province and its multi-scale processes. *Chinese Sci Bull* 67:997–1011. <https://doi.org/10.1360/tb-2021-0827>
- Liebmann B, Smith CA (1996) Description of a complete (interpolated) outgoing longwave radiation dataset. *Bull Am Meteorol Soc* 77:1275–1277
- Liu B, Yan Y, Zhu C et al (2020) Record-breaking Meiyu rainfall around the yangtze river in 2020 regulated by the subseasonal phase Transition of the North Atlantic oscillation. *Geophys Res Lett*. <https://doi.org/10.1029/2020GL090342>
- Liu H, Yan R, Wang B et al (2021) Multiscale combined action and disturbance characteristics of pre-summer extreme precipitation events over South China. *Adv Atmos Sci*. <https://doi.org/10.1007/s00376-021-1172-1>. View
- Liu F, Wang B, Ouyang Y et al (2022) Intraseasonal variability of global land monsoon precipitation and its recent trend. *Npj Clim Atmos Sci* 5:1–13. <https://doi.org/10.1038/s41612-022-00253-7>
- Liu X, Zhu Z, Lu R et al (2023) Unprecedented July rainfall in North China in 2021: combined effect of atlantic warming and Arctic sea-ice loss. *J Geophys Res Atmos* 128:1–13. <https://doi.org/10.1029/2022JD038068>
- Mao J, Wu G (2006) Intraseasonal variations of the Yangtze rainfall and its related atmospheric circulation features during the 1991 summer. *Clim Dyn* 27:815–830. <https://doi.org/10.1007/s00382-006-0164-2>
- Moon JY, Wang B, Ha KJ, Lee JY (2013) Teleconnections associated with Northern hemisphere summer monsoon intraseasonal oscillation. *Clim Dyn* 40:2761–2774. <https://doi.org/10.1007/s00382-012-1394-0>
- Nie Y, Sun J (2022) Moisture sources and transport for extreme precipitation over Henan in July 2021. *Geophys Res Lett*. <https://doi.org/10.1029/2021gl097446>
- Nie Y, Sun J (2023) Regional persistent extreme precipitation events over southwest china under different low-latitude intraseasonal oscillations during rainy season. *J Clim*. <https://doi.org/10.1175/jcli-d-22-0310.1>
- Ran L, Li S, Zhou Y et al (2021) Observational analysis of the dynamic, thermal, and water vapor characteristics of the “7.20” extreme rainstorm event in Henan Province, 2021. *Chinese J Atmos Sci* 45:1366–1383. <https://doi.org/10.3878/j.issn.1006-9895.2109.21160>
- Rao J, Xie J, Cao Y et al (2022) Record flood-producing rainstorms of July 2021 and august 1975 in Henan of China: comparative synoptic analysis using ERA5. *J Meteorol Res* 36:809–823. <https://doi.org/10.1007/s13351-022-2066-6>

- Ren P, Ren HL, Fu JX et al (2018) Impact of boreal summer intraseasonal oscillation on rainfall extremes in Southeastern China and its predictability in CFSv2. *J Geophys Res Atmos* 123:4423–4442. <https://doi.org/10.1029/2017JD028043>
- Ren Q, Liu F, Wang B et al (2022) Origins of the intraseasonal variability of East Asian summer precipitation. *Geophys Res Lett*. <https://doi.org/10.1029/2021GL096574>
- Reynolds RW, Smith TM, Liu C et al (2007) Daily high-resolution-blended analyses for sea surface temperature. *J Clim* 20:5473–5496. <https://doi.org/10.1175/2007JCLI1824.1>
- Su A, Lu X, Cui L et al (2021) The basic observational analysis of “7.20” extreme rainstorm in Zhengzhou. *Torrential Rain Disasters* 40:445–454
- Sun X, Jiang G, Ren X, Yang X (2016) Roles of intraseasonal oscillation in the persistent extreme precipitation over the Yangtze River basin during June 1998. *J Geophys Res Atmos* 121:10453–10469. <https://doi.org/10.1002/2016JD025077>
- Takahashi N, Hayasaka T (2020) Air-sea interactions among oceanic low-level cloud, sea surface temperature, and atmospheric circulation on an intraseasonal time scale in the summertime north Pacific based on satellite data analysis. *J Clim* 33:9195–9212. <https://doi.org/10.1175/JCLI-D-19-0670.1>
- Takaya K, Nakamura H (2001) A formulation of a phase-independent wave-activity flux for stationary and migratory quasigeostrophic eddies on a zonally varying basic flow. *J Atmos Sci* 58:608–627. [https://doi.org/10.1175/1520-0469\(2001\)058%3c0608:AFOAPI%3e2.0.CO;2](https://doi.org/10.1175/1520-0469(2001)058%3c0608:AFOAPI%3e2.0.CO;2)
- Trenberth KE (1991) Storm tracks in the Southern hemisphere. *J Atmos Sci* 48:2159–2178
- Wang X, Liu Y (2017) Causes of extreme rainfall in May 2013 over Henan Province: the role of the southwest vortex and low-level jet. *Theor Appl Climatol* 129:701–709. <https://doi.org/10.1007/s00704-017-2054-4>
- Wang B, Xie X (1997) A Model for the boreal summer intraseasonal oscillation. *J Atmos Sci* 54:72–86. [https://doi.org/10.1175/1520-0469\(1997\)054%3c0072:amftbs%3e2.0.co;2](https://doi.org/10.1175/1520-0469(1997)054%3c0072:amftbs%3e2.0.co;2)
- Wang L, Li T, Zhou T (2012) Intraseasonal SST variability and air-sea interaction over the kuroshio extension region during boreal summer. *J Clim* 25:1619–1634. <https://doi.org/10.1175/JCLI-D-11-00109.1>
- Wang L, Li T, Zhou T, Rong X (2013) Origin of the intraseasonal variability over the north Pacific in boreal summer. *J Clim* 26:1211–1229. <https://doi.org/10.1175/JCLI-D-11-00704.1>
- Wang Y, Ren HL, Wei Y et al (2022) MJO phase swings modulate the recurring latitudinal shifts of the 2020 extreme summer-monsoon rainfall around yangtse. *J Geophys Res Atmos* 127:1–15. <https://doi.org/10.1029/2021JD036011>
- Wu R, Kinter JL (2010) Atmosphere-ocean relationship in the midlatitude North Pacific: seasonal dependence and east-west contrast. *J Geophys Res Atmos* 115:1–12. <https://doi.org/10.1029/2009JD012579>
- Wu J, Li J, Zhu Z, Hsu PC (2023) Factors determining the subseasonal prediction skill of summer extreme rainfall over southern China. *Clim Dyn* 60:443–460. <https://doi.org/10.1007/s00382-022-06326-w>
- Xu H, Duan Y, Li Y, Wang H (2022a) Indirect effects of binary typhoons on an extreme rainfall event in Henan Province, China from 19 to 21 July 2021: 2. Numerical Study *J Geophys Res Atmos* 127:1–20. <https://doi.org/10.1029/2021JD036083>
- Xu H, Duan Y, Xu X (2022b) Indirect effects of binary typhoons on an extreme rainfall event in Henan province, China from 19 to 21 July 2021: 1 ensemble-based analysis. *J Geophys Res Atmos*. <https://doi.org/10.1029/2021JD036265>
- Xu L, Cheng W, Deng Z et al (2022c) Assimilation of the FY-4A AGRI clear-sky radiance data in a regional numerical model and its impact on the forecast of the “21-7” Henan extremely persistent heavy rainfall. *Adv Atmos Sci* 35:1–16. <https://doi.org/10.1007/s00376-022-1380-3>. View
- Yan Y, Zhu C, Liu B (2023) Subseasonal predictability of the July 2021 extreme rainfall event over Henan China in S2S operational models. *J Geophys Res Atmos* 128:1–17. <https://doi.org/10.1029/2022JD037879>
- Yang J, Wang B, Bao Q (2010) Biweekly and 21–30-day variations of the subtropical summer monsoon rainfall over the lower reach of the Yangtze river basin. *J Clim* 23:1146–1159. <https://doi.org/10.1175/2009JCLI3005.1>
- Yang S, Wu B, Zhang R, Zhou S (2013) The zonal propagating characteristics of low-frequency oscillation over the Eurasian mid-high latitude in boreal summer. *Sci China Earth Sci* 56:1566–1575. <https://doi.org/10.1007/s11430-012-4576-z>
- Yasunari T (1980) A quasi-stationary appearance of 30 to 40 Day period in the cloudiness fluctuations during the summer monsoon over India. *J Meteorol Soc Japan Ser II* 58:225–229. https://doi.org/10.2151/jmsj1965.58.3_225
- Yasunari T (1981) Structure of an Indian summer monsoon system with around 40-day period. *J Meteorol Soc Japan Ser II* 59:336–354. https://doi.org/10.2151/jmsj1965.59.3_336
- Yin J, Gu H, Liang X et al (2022) A Possible dynamic mechanism for rapid production of the extreme hourly rainfall in Zhengzhou City on 20 July 2021. *J Meteorol Res* 36:6–25. <https://doi.org/10.1007/s13351-022-1166-7>
- Zhang X, Yang H, Wang X et al (2021) Analysis on characteristic and abnormality of atmospheric circulations of the July 2021 extreme precipitation in Henan. *Trans Atmos Sci* 44:672–687. <https://doi.org/10.13878/j.cnki.dqkxxb.20210907001>
- Zhong R, Zhong L-H, Hua L-J, Feng S-D (2014) A Climatology of the Southwest vortex during 1979–2008. *Atmos Ocean Sci Lett* 7:577–583. <https://doi.org/10.3878/AOSL20140042>
- Zhu C, Nakazawa T, Li J, Chen L (2003) The 30–60 day intraseasonal oscillation over the western North Pacific ocean and its impacts on summer flooding in China during 1998. *Geophys Res Lett* 30:1952. <https://doi.org/10.1029/2003GL017817>

Publisher's Note Springer Nature remains neutral with regard to jurisdictional claims in published maps and institutional affiliations.

Springer Nature or its licensor (e.g. a society or other partner) holds exclusive rights to this article under a publishing agreement with the author(s) or other rightsholder(s); author self-archiving of the accepted manuscript version of this article is solely governed by the terms of such publishing agreement and applicable law.